Journal of Biomedical Optics

SPIEDigitalLibrary.org/jbo

# Photoacoustic/ultrasound dual-modality contrast agent and its application to thermotherapy

Yu-Hsin Wang
Ai-Ho Liao
Jui-Hao Chen
Churng-Ren Chris Wang
Pai-Chi Li

SPIE

Journal of Biomedical Optics 17(4), 045001 (April 2012)

# Photoacoustic/ultrasound dual-modality contrast agent and its application to thermotherapy

**Yu-Hsin Wang,[a,b] Ai-Ho Liao,[c] Jui-Hao Chen,[d] Churng-Ren Chris Wang,[d] and Pai-Chi Li[a,b]**
[a]National Taiwan University, Graduate Institute of Biomedical Electronics and Bioinformatics, Taipei 106, Taiwan
[b]National Taiwan University, Department of Electrical Engineering, Taipei 106, Taiwan
[c]National Taiwan University of Science and Technology, Graduate Institute of Biomedical Engineering, Taipei 106, Taiwan
[d]National Chung-Cheng University, Department of Chemistry and Biochemistry, Chia-Yi 621, Taiwan

**Abstract.** This study investigates a photoacoustic/ultrasound dual-modality contrast agent, including extending its applications from image-contrast enhancement to combined diagnosis and therapy with site-specific targeting. The contrast agent comprises albumin-shelled microbubbles with encapsulated gold nanorods (AuMBs). The gas-filled microbubbles, whose diameters range from submicrometer to several micrometers, are not only echogenic but also can serve as drug-delivery vehicles. The gold nanorods are used to enhance the generation of both photoacoustic and photothermal signals. The optical absorption peak of the gold nanorods is tuned to 760 nm and is invariant after microbubble encapsulation. Dual-modality contrast enhancement is first described here, and the applications to cellular targeting and laser-induced thermotherapy in a phantom are demonstrated. Photoacoustic imaging can be used to monitor temperature increases during the treatment. The targeting capability of AuMBs was verified, and the temperature increased by 26°C for a laser power of 980 mW, demonstrating the potential of combined diagnosis and therapy with the dual-modality agent. Targeted photo- or acoustic-mediated delivery is also possible.
[DOI: 10.1117/1.JBO.17.4.045001]

Keywords: dual modality; gold nanorods; microbubbles; laser-induced thermotherapy; theragnosis.

Paper 11292 received Jun. 8, 2011; revised manuscript received Feb. 12, 2012; accepted for publication Feb. 20, 2012;

## 1 Introduction

Photoacoustic (PA) imaging is a noninvasive and nonradioactive tool to assess the constituents inside tissue. A pulsed laser is typically used to irradiate the subject, and the absorption of the laser pulse energy by a chromophore induces local thermal expansion and produces a pressure transient. PA imaging is based on using the detected acoustic signals to reconstruct the optical absorption distribution. For biomedical applications, ultrasound (US) transducers are used to collect the generated wideband acoustic signals.[1,2] Since US and PA modalities share the same instrumentation, they are commonly paired with each other and have become a potent dual-modality method that provides complementary information. The high acoustic resolution of US imaging can provide fine morphological details, while PA imaging has better contrast and can be used to acquire functional information about hemoglobin and oxygen saturation for applications such as angiogenesis.[3]

Contrast agents for these two modalities have been studied separately. Microbubbles (MBs), which can be composed of phospholipids, albumin, or polymer, have been used clinically. Gas-filled MBs can produce strong acoustic scattering relative to surrounding tissue.[4] On the other hand, metallic nanoparticles, such as silver and gold, are usually applied to enhance the PA signal intensity.[5,6] They can be formed into different shapes. For example, gold nanorods (AuNRs) can be tuned to match the desired peak absorption based on their aspect ratio, and their peak optical absorption wavelength is typically set to be in the near infrared (NIR) region for biomedical applications.[2,6] However, MBs and AuNRs have significant difference in dimension (MB in $\mu$m and AuNR in nm), so their behavior in body could have discrepancy. Incorporation of both contrast agents ensures that AuNRs and MBs circulate together, thus they can be simultaneously detected.

In this paper, we propose a PA/US dual-modality contrast agent that comprises AuNRs encapsulated into MBs. Previous studies investigating such contrast agents have only considered signal enhancement without fully addressing their potential in other applications. For examples, nano-droplets containing liquid-form perfluorocarbon and gold nanospheres can improve dual-modal contrast after the optical trigger,[7] while the polymer-based MBs encapsulating India ink can generate PA/US signal in a more direct way.[8] Therefore, a major purpose of the proposed dual-modality contrast agent is designed for biomedical applications with NIR absorption and to extend the applications to specific-targeting and thermotherapy. Since the echogenic MBs can also be used as drug-delivery vehicles and, with appropriate molecular design, they can be targeted to specific cells.[9] In addition, a US-mediated method has been shown to improve the delivery efficiency of a drug, nanoparticles, or gene. The mechanism includes thermal effects, such as acoustic energy absorption, and mechanical effects, including cavitation, radiation force, and acoustic streaming.[10,11] On the other hand, the AuNRs allow for PA signal and photothermal therapy.[12,13] Specifically, laser-induced thermotherapy (LIT) can be applied and the temperature can be simultaneously monitored by PA imaging.[14,15] The temperature elevation leads to hyperthermia for therapy, which then causes cell necorsis. PA imaging of

---

Address all correspondence to: Pai-Chi Li, National Taiwan University, Department of Electrical Engineering and Graduate Institute of Biomedical Electronics and Bioinformatics, No. 1 Section 4 Roosevelt Road Taipei 106, Taiwan. Tel: +886-2-33663551; Fax: +886-2-83691354; E-mail: paichi@ntu.edu.tw.

0091-3286/2012/$25.00 © 2012 SPIE

AuNRs is used to monitor heating treatments, since the temperature can be directly derived from the changes in PA signals.[16–18] Previous studies have concluded that the signal intensity, which depends on the Grüenisen parameter ($\Gamma$), is linearly proportional to the temperature within the range from 10 to 55°C for soft tissue.[17] The derived temperature is expressed as follows:

$$T(z) = \left[\frac{a + bT_0(z)}{b}\right]\left[\frac{P(z)}{P_0(z)}\right] - \frac{a}{b}, \tag{1}$$

where $T_0$ and $P_0$ are the initial temperature and pressure, respectively, and constants $a$ and $b$ are related to the materials and the measurement environment; for example, $a = 0.016$ and $b = 0.0046$ for water (based on its thermal properties).[18]

Imaging agents, which were originally used for image-contrast enhancement, have been extended to recognize molecular characteristics and further provide therapeutic functions. Therapy combined with diagnosis, also known as theragnosis, is receiving increasing attention.[19,20] Furthermore, the multimodality imaging approach has great promise due to different imaging modalities providing complementary information.[20–23] The ideal approach to theragnosis should be noninvasive and allow real-time monitoring. There are various existing technologies. For example, PET/CT and PET/MRI were the first multimodality imaging systems to be commercialized, and they are now widely used. PA/US multimodality imaging provides another option and additional benefits over current imaging, with the combination of different contrast agents allowing theragnosis approaches to be developed.[2,24] For diagnosis, dual targeting is possible. For therapy, enhanced photothermal effect can also be expected. Modifying the surface of MBs with antibodies allows them to identify vascular endothelium receptor associated with angiogenesis that occurs in tumor growth and enhance their targeting efficiency to the cells when flowing in the bloodstream. Also, US-induced cavitation causes MB disruption and enhances vascular permeability through the endothelium layer, which improves the extravasation of AuNRs. The thermotherapy can thus be performed on the targeted region outside the vessel and avoid heat diffusion by blood flow. The retention period can also be extended by modifying the surface of AuNRs with specific antibody that provides a more effective way of multiple selective targeting.

This paper is organized as follows. First, the synthesis methods for the dual-modality agents, named AuMBs, are described. The contrast agent was made up of human serum albumin (HSA) and AuNRs. Previously AuNRs were modified by cystamine for conjugation of antibodies, and blockers such as thiol-PEG were attached to improve the biocompatibility.[2,25] Here, the thiol-PEG is replaced by HSA, which has free thiol groups ($\text{Cys}^{34}$), and an AuNR-HSA solution is prepared for AuMBs synthesis. Avidin can be added to the solution for preparation of targeted ones so that biotinylated antibodies could be bound on the surface through avidin–biotin linking.[4,26] Hence the agent is able to achieve molecular detection, such as of overexpressed VEGFR2 in tumor angiogenesis.[27] Previous study also demonstrated this kind of targeted MBs attaching to the specific cells and the increased retention period in tumor region with antibodies.[28] Second, the characteristics of AuMBs are described, including their acoustic and optical characteristics. The former is confirmed by particle analysis and ultrasound imaging, whereas the latter is assessed by optical attenuation and PA spectroscopy. Finally, the applications of the dual-modality molecular probe are presented. Specifically, the targeting efficiency was examined by flow cytometry and cell attachment, and LIT was conducted using a continuous-wave (CW) laser. Meanwhile, PA imaging was used to monitor temperature changes in the samples. The AuNR-enhanced photothermal effect results in hyperthermia inside the region of interest (ROI).

## 2 Materials and Methods

### 2.1 *Preparing AuMBs and Targeted AuMBs for Flow Cytometry and Cell Attachment*

AuNRs with peak absorption at 760 nm ($\text{AuNR}_{760}$) were modified with cystamine using a previously developed procedure.[29] The electrochemical synthesis method can provide high yield and stabilize the dispersibility of AuNRs in solution, which help the next steps of MB fabrication. Briefly, 10 mL of 0.4 M cystamine dihydrochloride and 10 mL of 16 mM nitric acid were added to the AuNR solution. The solution was aged for 30 min before being centrifuged twice with relative centrifugal force of 3420 rcf and 7695 rcf separately for 10 min each to remove excess cystamine. The cystamine modified AuNR usually shows a slight shift of absorption peak and can be restored by dispersing process with deionized water. Hence the absorption peak of cyst-AuNR is hardly changed. The concentration of cystamine-modified AuNRs was adjusted to 30 nM, which is derived from its molar extinction coefficient of the standard solution ($1.534 \times 10^9\ \text{M}^{-1}\text{cm}^{-1}$).

Next, the modified AuNRs and 20% human serum albumin (HSA; Octapharma, Vienna, Austria) were mixed at equal volumes of 0.33 mL for each and incubated for 24 h at 4°C. AuMBs were produced by using a digital sonicator (Model 102C, Branson, Danbury, CT) to sonicate the 5 mL diluted solution—which contained 1.32% HSA (w/v), 1.98 nM $\text{AuNR}_{760}$, and perfluorocarbon ($C_3F_8$) gas—for 2 min.

AuMBs of different sizes were then stratified by varying the centrifuge acceleration, with larger (AuMB1) and smaller (AuMB2) ones being collected after centrifugation with relative centrifugal force of 126 rcf for 2 min and 2754 rcf for 5 min, respectively.[30] The freshly prepared AuMBs were examined. The concentration of the solution and particle size distribution were measured by a size-analysis device (Multisizer 3, Beckman Coulter, San Jose, CA) using a 30-$\mu$m aperture. Some of the AuMBs were filtered with a 5-$\mu$m syringe filter (Sartorius, Goettingen, Germany) and then hardened using 2.5% glutaraldehyde. A transmission electron microscope (TEM, H7100, Hitachi, Tokyo, Japan) was used to investigate the morphology of the hardened AuMBs at an accelerating voltage of 100 kV.

To produce the targeted AuMBs, avidin was added prior to sonication for synthesis. The avidin-incorporated AuMBs was prepared by sonicating the solution, which contains 1.98 nM AuNR, 1.32% HSA, 0.04% (w/v) avidin. The synthesis procedure is similar to the description above for preparation of AuMBs except the addition of avidin. Next, the AuMBs were washed three times to remove the free avidin. The targeting ability was examined by incubating the samples with biotin-FITC (eBioscience, San Diego, CA) for 30 min. The biotin-FITC–avidin-conjugated AuMBs were washed three times to remove the unbound fluorophores. Flow cytometry (FACSAria II, Becton Dickinson, San Jose, CA) was used to examine the targeting efficacy of the produced AuMBs.

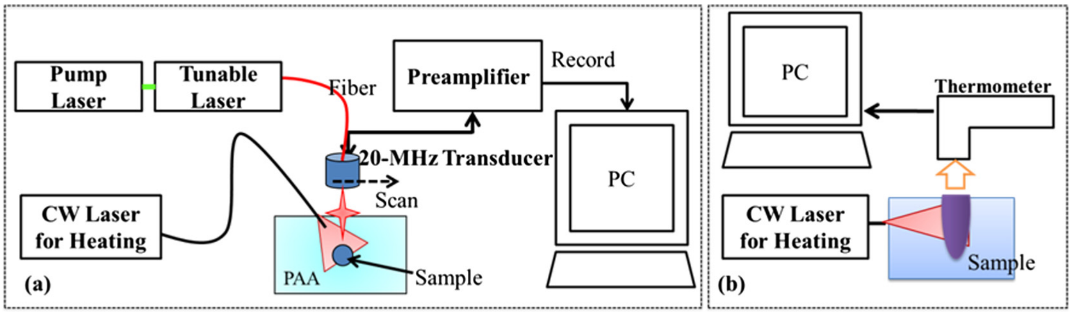

**Fig. 1** Experimental setups of measurements employing the PA/US agent: (a) dual-modality imaging system and CW laser for LIT, and (b) temperature measurement during LIT.

On the other hand, biotinylated antimouse VEGFR2 (eBioscience, San Diego, CA) was incubated with avidin-incorporated AuMBs for 30 min. Three washes were performed to remove unbound antibodies. These anti-VEGFR2-avidin-conjugated AuMBs were then used to assess their attachment to the specific receptor. Mouse endothelium bEnd.3 cells purchased from the American Tissue Culture Collection (ATCC, Manassa, VA) were grown in Dulbecco's modified Eagle's medium. With 10-min exposure to 3 mL of AuMBs at a concentration of $0.7 \times 10^7$ microbubbles per milliliter, the cells were washed by PBS to remove the unbound ones. For each group, five plates of cells were examined, and the microscopic pictures were taken randomly.

## 2.2 *Experimental Setup of the Imaging System and LIT*

Figure 1 shows the experimental setup of the dual-modality imaging system and direct temperature measurements during LIT. In the imaging experiments, four groups of samples

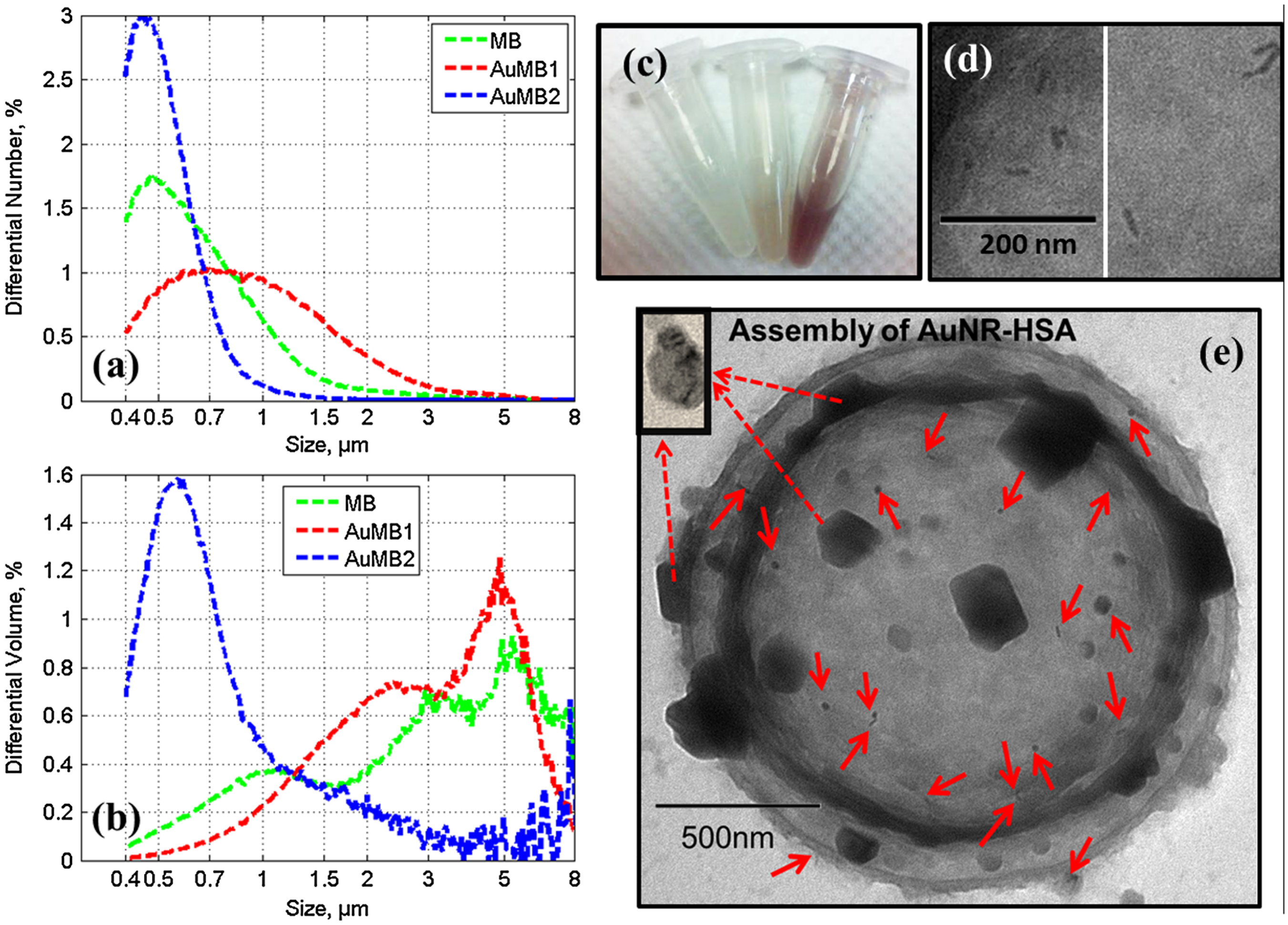

**Fig. 2** Size distributions of MBs (green), AuMB1 (red), and AuMB2 (blue) for the differential number (a) and the differential volume (b). (c) Photograph of MBs, AuMB1, and AuMB2 (from left to right). TEM images of AuNRs in AuMB (d) and AuMB1 (e) where red arrows indicate single AuNRs and dashed ones point to assemblies of AuNR and HSA.

(MB, AuNR, AuMB1, and AuMB2) were separately embedded into polyacrylic acid (PAA) gel at a depth of around 12 mm. The PAA gel was prepared by adding 3 $\mu$L of 10% APS solution to per mL of acrylamide solution. The sound velocity in the phantom was 1595 m/s at room temperature.[31] The samples were irradiated by a Ti:sapphire laser (CF-125, SOLAR TII, Minsk, Belarus) that uses an Nd:YAG laser as the pump (LS-2137 U, LOTIS TII, Minsk, Belarus). The pulse duration of laser is around 15 ns, and the repetition frequency is 10 Hz. This tunable laser can provide excitation at wavelengths ranging from 700 to 980 nm and hence was suitable for our study. A custom 20-MHz fiber-integrated transducer was used for detection, with the PA or US signal being sent to a preamplifier (5077PR, Panametrics, Waltham, MA). The transducer was mounted on a precision translation stage, and B-scan images in $x-z$ plane were obtained by moving the driving motor (HR-8, Nanomotion, Yokneam, Israel) with a step size of 0.02 mm. These images were recorded by a data acquisition card (CompuScope 14200, Gage, Lachine, QC, Canada) in a PC at 100 MHz. All PA images were formed using a laser pulse fluence of around 8 mJ/cm$^2$.

LIT was performed using an 808-nm CW diode laser (ONSET Electro-optics, Taipei, Taiwan) operating at 980 mW. Figure 1(a) shows the use of PA imaging for monitoring the treatment, while Fig. 1(b) shows how an infrared thermometer (Optris LS, Optris, Berlin, Germany) was used to record the temperature rise of the sample placed in the agarose gel for comparison. In the thermal treatment, the pressure ratio was acquired from PA intensity differences between two images obtained before and during heating and thus assessed the temperature. To avoid sound-velocity variations, the position of the object has to be corrected by comparing two images in advance.

## 3 Results

### 3.1 *Particle Analysis and TEM*

The concentration of AuMBs was measured for each production batch. Our protocols using 1.32% (w/v) HSA typically produce $3.5 \sim 3.8 \times 10^9$ MBs/mL. Figs. 2(a) and 2(b) show the size distributions as a function of the differential number and volume, respectively, for AuMB1, AuMB2, and MB. The AuMB1 group contained a greater proportion of MBs with sizes up to several micrometers, while most of the MBs in the AuMB2 group were smaller than 0.7 $\mu$m. The figure indicates the presence of only one peak in the differential volume at about 0.6 $\mu$m for AuMB2, while there were two peaks (i.e., at 2.5 and 5 $\mu$m) for AuMB1. The MBs exhibited the expected size diversity without stratification. There are differences in the volume, which leads to a smaller buoyancy for AuMB2 and hence a higher acceleration being needed during centrifugation. Figure 2(c) is a photograph of three samples of MBs, AuMB1, and AuMB2. TEM images are also shown in Figs. 2(d) and 2(e) for the incorporated nanorods and the hardened AuMB1, respectively. These images directly display the dimensions of the MBs and their contents. The AuNR tends to submerge into the bubbles from our TEM observation, which might be the most stable form in liquid. In addition, the microscopic images suggested that there were several tens of AuNRs per AuMBs, and some of them assembled with HSA, which made it difficult to assess the exact number. In Fig. 2(e), red arrows indicate single AuNRs, which can be seen more clearly in (d), and dashed arrows point to part of the assemblies. The enlarged views were captured to demonstrate locations of AuNR and the contents of AuNR-HSA assemblies. We assume that the dispersed nanorods and the AuNR-HSA assemblies were randomly located in the microbubble to evaluate the number of

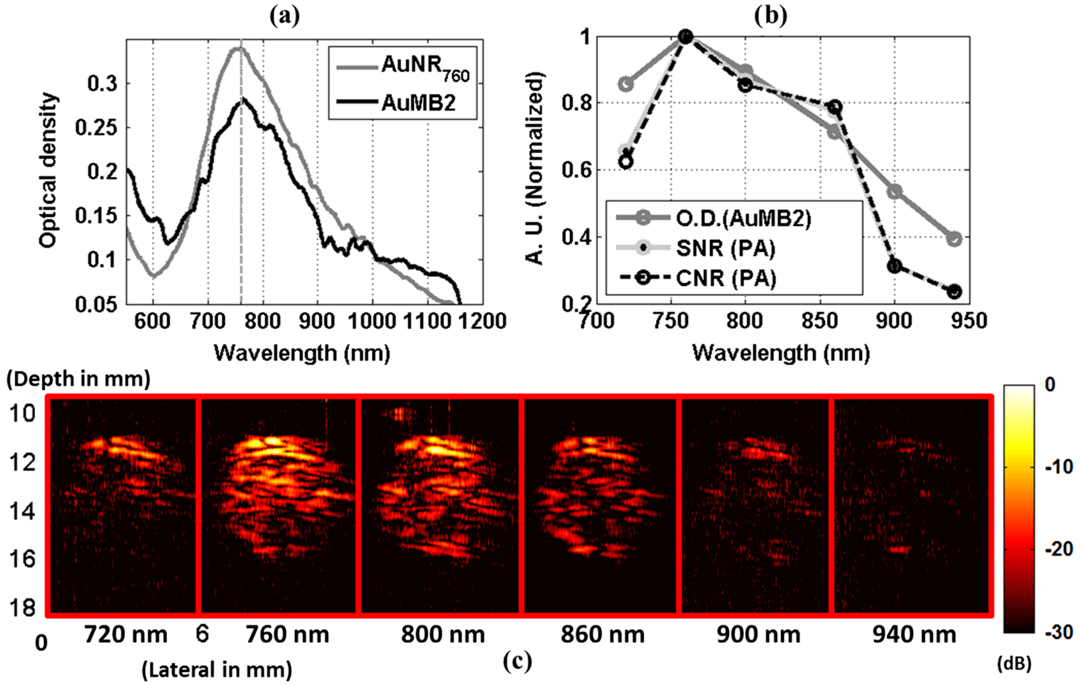

**Fig. 3** (a) Optical density of AuMB2 (black) and AuNR$_{760}$ (gray), (b) Comparison of normalized optical density (dark gray), SNR (light gray), and CNR (black dotted) in PA images of AuMB2, (c) PA spectroscopy of AuMB2.

nanoparticles. For the assemblies, there were five (or more) AuNRs inside [inset of Fig. 2(e)]. For the dispersed nanorods, there were approximately 20 rods observed in the scope. As there were approximately $3.8 \times 10^9$ MBs per mL, the concentration of AuNRs in the solution may ranges from 0.1 to 0.5 nM (30 AuNRs to 80 AuNRs per microbubble).

## 3.2 *PA Characteristics*

Figure 3 shows the optical absorption characteristics of dual-modality contrast agents, as assessed by the optical density [Fig. 3(a)] and PA spectroscopy [Figs. 3(b) and 3(c)]. The optical density was measured by double-integrating spheres and a spectrometer (USB4000, Ocean Optics, Largo, FL). Both absorption and scattering effects contribute to the attenuation, with scattering being especially exhibited by a foam-like liquid such as MBs but is less apparent for an AuNR solution. Figure 3(a) indicates that the peak of AuMB2 is consistent with that of $\mathrm{AuNR}_{760}$, which implies invariance of the optic absorption of the contrast agent. The increased attenuation at 550 nm is due to HSA. The diluted AuMB2 (~25%) has optical density 0.28 with half-centimeter path length at the wavelength 760 nm as shown. From macroscopic observation, the optic density of 25% AuMB2 had 0.2 higher (per cm) than MBs at the wavelength, which suggested that 0.52 nM AuNR were in the solution.

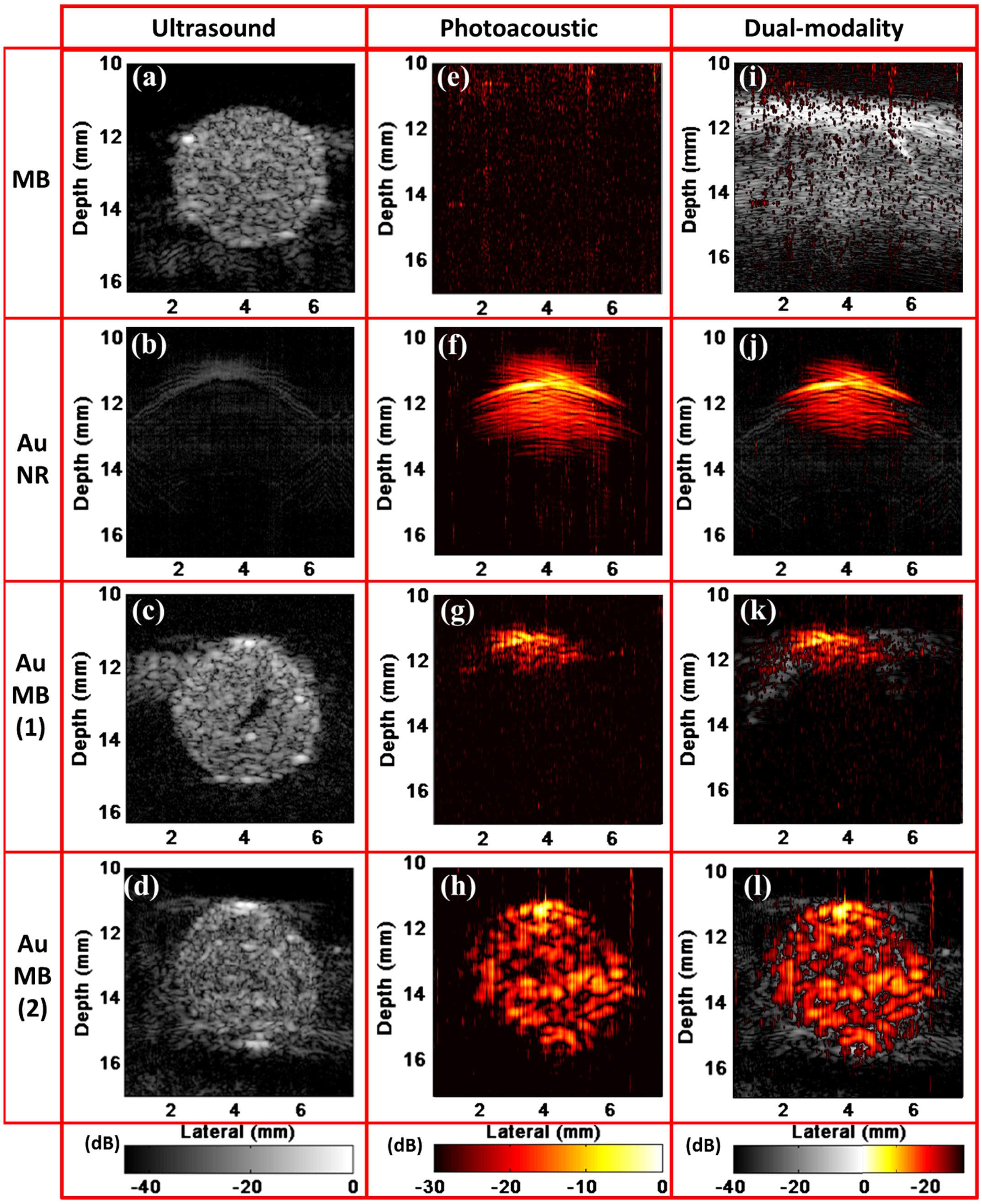

**Fig. 4** Images of contrast agents: (a to d) US images of 1% MB, 2 nm AuNR, 1% AuMB1, and 50% AuMB2; (e to h) PA images of 100% MB, 2 nm AuNR, 75% AuMB1, and 50% AuMB2; and (i to l) fused images of 100% MB, 2 nm AuNR, 75% AuMB1, and 50% AuMB2, where the US and PA data are in grayscale and thermal color, respectively.

PA spectroscopy involved varying the excitation wavelength from 720 to 940 nm. Figure 3(b) compares the optical density, signal-to-noise ratio (SNR) and the contrast-to-noise ratio (CNR) of AuMB2. The SNRs and CNRs were derived from the PA images shown in Fig. 3(c). The SNR compares the intensity in the ROI to the background, while CNRs are the SNRs normalized by the background standard deviation to eliminate variations in the laser output. The SNRs were 8.89, 13.55, 11.72, 10.50, 4.23, and 3.22 dB and the corresponding CNRs were 1.531, 2.447, 2.085, 1.932, 0.765, and 0.573 at wavelengths of 720, 760, 800, 860, 900, and 940 nm, respectively. Both the SNR and CNR resemble the values expected for optical density, except for less scattering at longer wavelengths. The dual-modality contrast agent had a peak absorption at 760 nm as expected.

## 3.3 *Dual-Modality Imaging*

US and PA images of the contrast agents are shown in Fig. 4: Figs. 4(a)–4(d), are the US images, Figs. 4(e)–4(h), are the PA images, and Figs. 4(i)–4(l), are the dual-modality images. Four sample types (1% MB, 2 nM AuNR, 1% AuMB1, and 50% AuMB2; diluted by agarose) are shown in the US images, which illustrate that the MBs and AuMB1 exhibited considerably enhanced contrast at the same concentration, whereas AuNR produced little pulse-echo. The higher concentration needed for AuMB2 was due to the particles being much smaller, which implies that they contain less gas. In fact, 10% AuMB2 could provide sufficient enhancement in the experiments (not shown). PA images of four other samples (100% MB, 2 nM AuNR, 75% AuMB1, and 50% AuMB2) are also presented. Note that the concentrations for MB and AuMB1 were higher for effective PA generation. With an excitation wavelength of 760 nm there was virtually no PA signal from the MBs, whereas the AuNR group had high absorption and generated PA signal efficiently. Both AuMBs with encapsulation of $\mathrm{AuNR}_{760}$ exhibited strong PA signals. The contrast for AuMB1 was dominant in the upper ROI since the optical scattering impedes the light penetration, while AuMB2 provided more-uniform enhancement. Dual-modality images of the samples (100% MB, 2 nM AuNR, 75% AuMB1, and 50% AuMB2) are displayed as grayscale US images overlaid with PA images in thermal color. The higher concentration of larger-size bubbles leads to acoustic shadowing, which was evident in (i) 100% MB and (k) 75% AuMB1 samples. Because of acoustic shadowing, the inclusion in the US images became less visible than that in the low concentration images [i.e., (a) and (c)]. Hence, the smaller AuMB2 is more suitable as the dual-modality contrast agent than AuMB1, which has larger size and higher concentration.

## 3.4 *Targeted Efficacy and LIT*

Surface bioconjugation extends the contrast agents to molecular probes. Flow cytometry was used to analyze the binding of the biotin-FITC to the MBs/AuMBs and to the avidin-incorporated MBs/AuMBs. Both of these sample types were mixed with biotin-FITC at an equivalent concentration and then washed as described in Sec. 2.1. Figure 5 shows example histograms of the fluorescence intensity (FI), with and without avidin conjugation, for MBs (as the control group) [Fig. 5(a)], AuMB1 [Fig. 5(b)] and AuMB2 [Fig. 5(c)]. An increased mean FI, as indicated by a shift of the distribution to the right, confirms more ligand binding of biotin-FITC on the MB surface. The increase in FI with FITC was greater for MBs and AuMBs conjugated with avidin. These results indicate that avidin can be incorporated into the shell of MBs and AuMBs during sonication and serve as a direct ligand for biotinylated antibodies. Quantitative analysis shows that the geometric mean FI was more than twofold higher for avidin-incorporated AuMB1 (124.09) than for nontargeted AuMB1 (50.94), and that the mean FI of avidin-incorporated AuMB2 was increased by more than 50% (from 235.01 to 371.80). This demonstrated

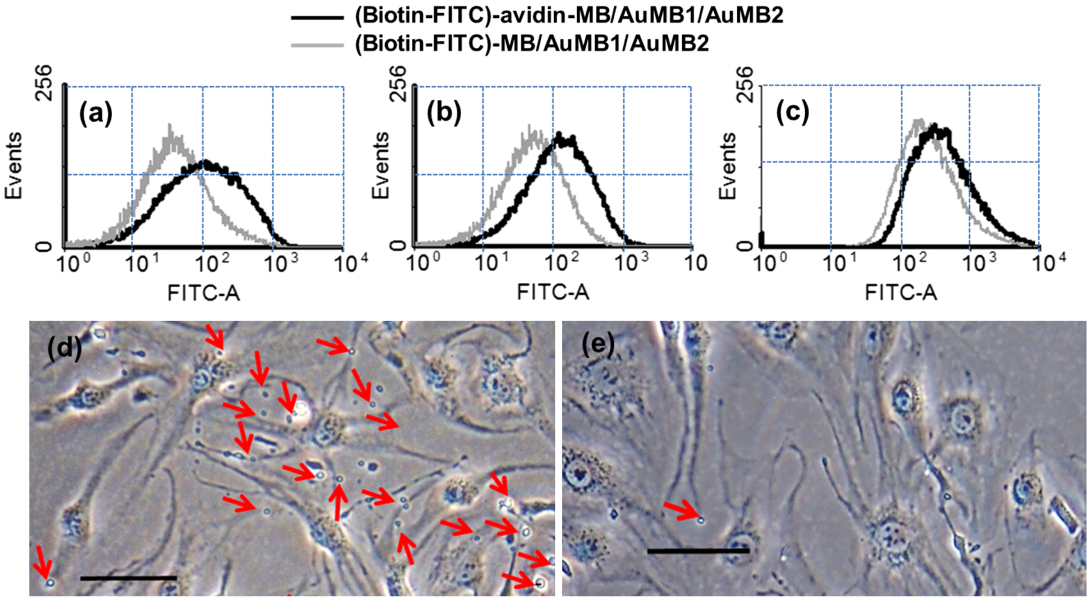

**Fig. 5** Flow-cytometry FI histograms of MB, AuMB1, and AuMB2 with (black) and without (gray) avidin conjugation: (a) avidin-MB conjugated with biotin-FITC; (b) avidin-AuMB1 conjugated with biotin-FITC; and (c) avidin-AuMB2 conjugated with biotin-FITC. (d) The microscopic picture of anti-VEGFR2-avidin-incoroprated AuMBs and mouse endotheliual cells (bEnd.3). (e) The control group. Arrows point to MBs that attached to the cells. (Original magnification: 200×, bar: 35 $\mu$m.)

usefulness of the AuMBs for PA/US dual-modality molecular imaging is expected to lead to therapeutic applications. [Fig. 5(d)] shows a picture of AuMBs attachment (red arrows) to mouse endothelium cells (bEnd.3) after a 10-min incubation and three washes. Cell contour can be observed in the images, and the number of cells and AuMB adhesion are confirmed. The AuMBs can be identified by the image intensity, size, and locations or directly seen in bright-field image. The bEND.3 cell is known for their VEGFR2 expression. With anti-VEGFR2 bound on avidin-incorporated AuMBs, the conjugation with cellular receptor was observed ($0.92 \pm 0.19$ targeted AuMBs per cell), whereas MBs without antibodies can be easily washed out ($0.03 \pm 0.01$ AuMBs per cell, $p < 0.05$). The control group is shown in Fig. 5(e).

Finally, we present the results of LIT with the dual-modality contrast agents. Figure 6 shows the temperature rise measured by an infrared thermometer [Fig. 6(a)] and monitored by PA imaging [Figs. 6(b) and 6(c)]. The LIT employed a 980-mW CW laser to heat the samples. For the data shown in Fig. 6(a), an Eppendorf-shaped pit inside the agarose base was sequentially loaded with 1.5 mL of water, MB, 1.8 nM AuNRs, and AuMBs (without dilution), which can directly compare the abilities of the samples as a heat source. The AuNR concentration of 1.8 nM, as the control group, is closer to that of the solution before sonication (~1.92 nM), thus it was used to evaluate the efficiency. As the CW laser was switched on for the first 660 sec and then turned off, a temperature rise was clearly evident for AuNR and AuMBs, while the temperature of the water and MBs hardly changed. Although the optical absorbance of AuMB2 suggests that there were fewer nanorods inside compared with the 1.8 nM AuNR sample, it can be observed that the slight scattering of AuMB2 helps accumulate the optical energy. Whereas AuNRs suspended in water had lower increased temperature than expectation may result from the thermal diffusivity by water and energy penetration. Besides, the temperature increase was more than twofold greater for AuMB2 than for AuMB1 under the same conditions. The strong scattering caused by large bubbles impedes penetration of light. On the other hand, the increased temperature in AuMB2 is mostly because the ratio of AuNRs is greater for its smaller size. Note that AuNR adsorbs with HSA before the sonication, and AuMBs are filled most with gas. Besides, in equal volumes of solutions there may be more small-sized AuMB2, which can also be observed in our particle analysis results. Hence compared with AuMB1, AuMB2 is more efficient in photothermal therapy due to more AuNRs included and more uniform illumination for heating.

Figure 6 also provides PA-monitored thermal images of 75% AuMB1 [Fig. 6(b)] and 50% AuMB2 [Fig. 6(c)] inside the PAA phantom and immersed in water. Different concentrations of embedded samples were used for image quality to compare the PA intensity variation. After the CW laser was turned on, the average intensity increased by 3.35 and 6.02 dB for AuMB1 and AuMB2, respectively. For an initial temperature of 22.8°C, the results imply that the temperature would rise to around 35°C for AuMB1 and to 49°C for AuMB2 in a water-filled environment. In this case, the temperature increase was higher for AuMB2 than for AuMB1 and slightly exceeded what we observed in our previous experiment. Two possible reasons for this discrepancy are (1) underestimation by the infrared thermometer because it only measures the surface temperature and (2) local overestimation in the PA images due to the smaller specific heat of the metallic nanoparticles. It is evident that AuMB2 can help increase the temperature more with fewer amounts and that AuMBs are capable heat sources. Moreover, it is noteworthy that the experimental thermal images indicate that the temperature increase was concentrated in the ROI (not in the surroundings), which supports that LIT can be enhanced by AuMBs.

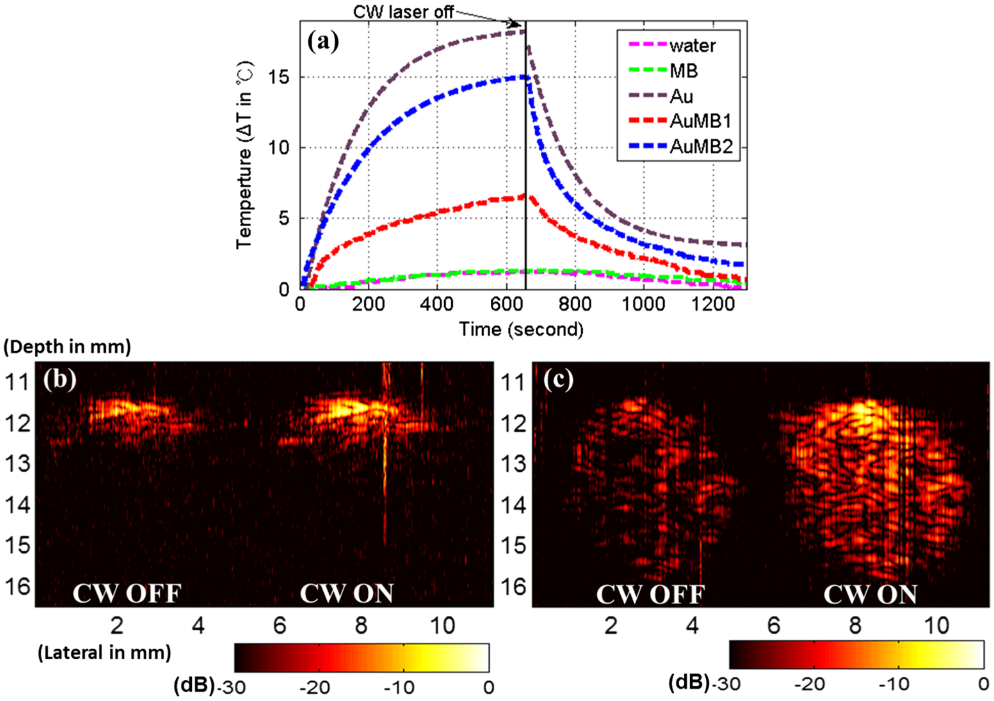

**Fig. 6** Temperature changes in contrast-agent samples during LIT. (a) Temperature rise measured by an infrared thermometer (magenta, water; green, MB; purple, AuNR; red, AuMB1; and blue, AuMB2). (b) (c) Thermal images obtained by PA imaging for a 75% AuMB1 phantom (b) and a 50% AuMB2 phantom (c).

## 4 Discussion and Conclusions

The present study synthesized dual-modality contrast agents, AuMBs, with HSA and encapsulated $\mathrm{AuNR}_{760}$. To our knowledge, this is the first work on extending this type of dual-modality contrast agent to molecular probe based on the fact that albumin shell allows for ligand binding to gold and antibodies. In terms of their optical characteristics, attenuation measurements and PA spectroscopy suggested that their peak absorption was invariant at 760 nm. The optical absorption peak within NIR indicates them suitable for biological tissue since this range is known as optical window in biological tissue. Moreover, AuMBs with different sizes were separated by centrifugation, as confirmed by particle analysis. The PA/US images show that AuMB2 can be an effective dual-modal contrast agent with a sufficiently high concentration. Both AuMBs were examined for their targeting ability and employed in LIT. The flow-cytometry results showed increased fluorescence in avidin-incorporated MBs, which suggest they could be used as molecular probes for targeted diagnoses and the cell attachment of AuMBs. The results obtained by an infrared thermometer and PA images in LIT experiments revealed temperature rises in the AuMBs, indicating they are suitable for inducing hyperthermia and also for providing enhanced treatment. Thus the PA/US dual-modality agents are not only able to provide contrast enhancement but also could serve as versatile theragnosis agents.

With sufficient understanding of their acoustic, thermal, and optical characteristics by qualitative and quantitative evaluations, full potential can then be exploited. For example, delivery of such agents can be directly improved by ultrasound cavitation.[32,33] Inertial cavitation by microbubble can increase extravasation of AuNRs and radiation force can increase accumulation of AuNRs. Also note that the cystamine remaining on the AuNR, which can be expected to provide antibody modification for dual-targeting and extending the retention period. Their dual properties can provide photo-triggered or US-mediated methods that further expand the potential applications in biomedicine.

## Acknowledgments

The authors thank Dr. Chung-Liang Chien for providing the transmission electron microscope, Dr. Eric Y. Chuang for helping cell culture, and Chia-Yu Lin for technical assistance. This research was partially funded by the National Science Council of Taiwan under grant NSC 99-3011-P-002-006.

## References

1. J. H. Liu et al., "Design, fabrication and testing of a dual-band photoacoustic transducer," *Ultrason. Imag.* **30**(4), 217–227 (2008).
2. P. C. Li et al.,"*In vivo* photoacoustic molecular imaging with simultaneous multiple selective targeting using antibody-conjugated gold nanorods," *Opt. Express* **16**(23), 18605–18615 (2008).
3. H. F. Zhang et al.,"Functional photoacoustic microscopy for high-resolution and noninvasive in vivo imaging," *Nat. Biotechnol.* **24**(7), 848–851 (2006).
4. K. Ferrara, R. Pollard, and M. Borden, "Ultrasound microbubble contrast agents: fundamentals and application to gene and drug delivery," *Annu. Rev. Biomed. Eng.* **9**, 415–447 (2007).
5. K. Homan et al., "Silver nanosystems for photoacoustic imaging and image-guided therapy," *J. Biomed. Opt.* **15**(2), 021316-1–021316-9 (2010).
6. M. Eghtedari et al., "High sensitivity of in vivo detection of gold nanorods using a laser optoacoustic imaging system," *Nano Lett.* **7**(7), 1914–1918 (2007).
7. K. Wilson, K. Homan, and S. Emelianov, "Photoacoustic and ultrasound imaging contrast enhancement using a dual contrast agent," *Proc. SPIE* **7564**, 75642P-1–75642P-5 (2010).
8. C. Kim et al., "Multifunctional microbubbles and nanobubbles for photoacoustic and ultrasound imaging," *J. Biomed. Opt.* **15**(1), 010510-1–010510-3 (2010).
9. W. G. Pitt, G. A. Husseini, and B. J. Staples, "Ultrasonic drug delivery—a general review," *Expert Opin. Drug Deliv.* **1**(1), 37–56 (2004).
10. S. Paliwal and S. Mitragotri, "Ultrasound-induced cavitation: applications in drug and gene delivery," *Expert Opin. Drug Deliv.* **3**(6), 713–726 (2006).
11. A. F. H. Lum et al., "Ultrasound radiation force enables targeted deposition of model drug carriers loaded on microbubbles," *J. Contr. Release* **111**(1–2), 128–134 (2006).
12. X. Huang et al., "Cancer cell imaging and photothermal therapy in near-infrared region by using gold nanorods," *J. Am. Chem. Soc.* **128**(6), 2115–2120 (2006).
13. J. L. Li and M. Gu, "Gold-nanoparticle-enhanced cancer photothermal therapy," *IEEE J. Sel. Top. Quant. Electron.* **16**(4), 989–996 (2010).
14. R. O. Esenaliev et al., "Real-time optoacoustic monitoring of temperature in tissues," *Proc. SPIE* **3601**, 268–275 (1999).
15. R. O. Esenaliev et al., "Laser optoacoustic technique for real-time measurement of thermal damage in tissues," *Proc. SPIE* **3594**, 98–109 (1999).
16. J. Kandulla et al., "Noninvasive optoacoustic online retinal temperature determination during continuous-wave laser irradiation," *J. Biomed. Opt.* **11**(4), 041111-1–041111-15 (2006).
17. J. Shah et al., "Photoacoustic imaging and temperature measurement for photothermal cancer therapy," *J. Biomed. Opt.* **13**(3), 034024-1–034024-9 (2008).
18. S. H. Wang et al., "Photoacoustic temperature measurements for monitoring of thermal therapy," *Proc. SPIE* **7177**, 71771S-1–71771S-11 (2009).
19. K. Kim et al., "Tumor-homing multifunctional nanoparticles for cancer theragnosis: simultaneous diagnosis, drug delivery, and therapeutic monitoring," *J. Contr. Release* **146**(2), 219–227 (2010).
20. G. M. Lanza et al., "Theragnostics for tumor and plaque angiogenesis with perfluorocarbon nanoemulsions," *Angiogenesis* **13**(2), 189–202 (2010).
21. A. H. Liao and P. C. Li, "The role of high frequency ultrasound in multimodality small animal imaging for cancer research," *J. Med. Ultrasound* **17**(2), 86–97 (2009).
22. R. Olafsson et al., "Real-time, contrast enhanced photoacoustic imaging of cancer in a mouse window chamber," *Opt. Express* **18**(18), 18625–18632 (2010).
23. A. Louie, "Multimodality imaging probes: design and challenges," *Chem. Rev.* **110**(5), 3146–3195 (2010).
24. G. E. R. Weller et al., "Targeted ultrasound contrast agents: in vitro assessment of endothelial dysfunction and multi-targeting to ICAM-1 and sialyl Lewis$^x$," *Biotechnol. Bioeng.* **92**(6), 780–788 (2005).
25. Y. Akiyama et al., "The effects of PEG grafting level and injection dose on gold nanorod biodistribution in the tumor-bearing mice," *J. Contr. Release* **139**(1), 81–84 (2009).
26. A. L. Klibanov et al., "Targeting and ultrasound imaging of microbubble-based contrast agents," *MAGMA* **8**(3), 177–184 (1999).
27. N. Deshpande, M. A. Pysz, and J. K. Willmann, "Molecular ultrasound assessment of tumor angiogenesis," *Angiogenesis* **13**(2), 175–188 (2010).
28. J. K. Willmann et al., "Dual-targeted contrast agent for US assessment of tumor angiogenesis in vivo," *Radiology* **248**(3), 936–944 (2008).
29. Y. Y. Yu et al., "Gold nanorods: electrochemical synthesis and optical properties," *J. Phys. Chem. B* **101**(34), 6661–6664 (1997).
30. J. A. Feshitan et al., "Microbubble size isolation by differential centrifugation," *J. Colloid Interface Sci.* **329**(2), 316–324 (2009).
31. A. F. Prokop et al., "Polyacrylamide gel as an acoustic coupling medium for focused ultrasound therapy," *Ultrasound Med. Biol.* **29**(9), 1351–1358 (2003).
32. Y.-H. Chuang et al., "Effects of ultrasound-induced inertial cavitation on enzymatic thrombolysis," *Ultrason. Imag.* **32**(2), 81–90 (2010).
33. C.-Y. Lai et al., "Quantitative relations of acoustic inertial cavitation with sonoporation and cell viability," *Ultrasound Med. Biol.* **32**(12), 1931–1941 (2006).